

Supporting Information for

## Interfacial Electronic Modulation of Dual-Monodispersed Pt-Ni<sub>3</sub>S<sub>2</sub> as Efficacious Bi-functional Electrocatalysts for Concurrent H<sub>2</sub> Evolution and Methanol Selective Oxidation

Qianqian Zhao<sup>1</sup>, Bin Zhao<sup>1,\*</sup>, Xin Long<sup>1</sup>, Renfei Feng<sup>2</sup>, Mohsen Shakouri<sup>2</sup>, Alisa Paterson<sup>2</sup>, Qunfeng Xiao<sup>2</sup>, Yu Zhang<sup>3</sup>, Xian-Zhu Fu<sup>1</sup>, Jing-Li Luo<sup>1,\*</sup>

<sup>1</sup> Shenzhen Key Laboratory of Energy Electrocatalytic Materials, Shenzhen Key Laboratory of Polymer Science and Technology, Guangdong Research Center for Interfacial Engineering of Functional Materials, College of Materials Science and Engineering, Shenzhen University, Shenzhen 518060, P. R. China

<sup>2</sup> Canadian Light Source Inc., Saskatoon, S7N 0X4, Saskatchewan, Canada

<sup>3</sup> Instrumental Analysis Center of Shenzhen University (Lihu Campus), Shenzhen University, Shenzhen, Guangdong 518055, P. R. China

\*Corresponding authors. E-mail: [bin.zhao@szu.edu.cn](mailto:bin.zhao@szu.edu.cn) (Bin Zhao), [jll@szu.edu.cn](mailto:jll@szu.edu.cn) (Jing-Li Luo)

### S1 Method

#### S1.1 Chemicals

All the reagents were used as received without further purification, including nickel (II) acetylacetonate (Ni(acac)<sub>2</sub>; 96%), Platinum(II) acetylacetonate (Pt(acac)<sub>2</sub>; 98%), diphenyl disulfide (DPDS; 96%), oleylamine (OLA; 90%) and Nafion solution (~5% in a mixture of lower aliphatic alcohols and water) were purchased from Sigma-Aldrich. KOH (GR, 95%), Toluene (AR, 99.5%), methanol (AR, 99.5%), and isopropanol (AR, 99.5%) were obtained from Sinopharm Chemical Reagent Co. Ltd. (Shanghai, China) and commercial 20% Pt/C obtained from Aladdin Chemical Reagent Co. Ltd. (Shanghai, China). All chemicals were used as received without any further purification.

#### S1.2 Synthesis of Ni<sub>3</sub>S<sub>2</sub> catalyst

The one-pot solution-based syntheses were performed using a standard *Schlenk* vacuum line technique under argon atmosphere. In a standard synthesis, 2 mmol (0.5138 g) Ni(acac)<sub>2</sub> and OLA (20 mL) were fully dissolved in a round-bottom *Schlenk* flask (100 mL) at room temperature. The flask was degassed under vacuum at 80 °C for 0.5 h to remove oxygen and other low-boiling-point organic solvents in oil bath. Subsequently, the reaction was programmed to be 220 °C with a ramp of 5 °C min<sup>-1</sup> after backfilling with Ar in oil bath. At the same time, 1 mmol (0.2184 g) DPDS and 3 mL OLA, 0.1 mmol (0.04 g) Pt(acac)<sub>2</sub> and 1 mL OLA was separately mixed in a glass vial, then preheated to 80 °C on a hot plate to form a clear solution. When the flask reaches 220 °C, the diphenyl disulfide solution was injected into the metal solution by syringe. After injection, the temperature drops to 210-215 °C and the reaction was allowed to maintain at 215 °C for 10 minutes with continuous stirring. After stopping the reaction, the flask was taken out of the oil bath and allowed to naturally cool to room

temperature. The product was dissolved in toluene and the solution was centrifuged at 12000 rpm during 10 minutes for nanoparticles separation. Finally, the as-synthesized Ni<sub>3</sub>S<sub>2</sub> nanocrystals were thoroughly purified by multiple precipitation and re-dispersion steps using toluene and isopropanol.

### 1.3 Preparation of Working Electrode

The Pt-Ni<sub>3</sub>S<sub>2</sub> catalyst modified carbon cloth is employed as both cathode and anode electrodes. Prior to the modification, carbon cloth (CC) was cut into 0.5 cm × 1.5 cm rectangular pieces, and then they were rinsed with water and ethanol thoroughly under sonication to remove residual organic species. For electrode modification, we use fresh suspensions to prepare ink by the following steps: the toluene suspension (1 mL) was separately dissolved in isopropanol and ethanol, and the solution was centrifuged at 10000 rpm during 5 minutes to precipitate metal complexes. Then the as-synthesized Pt-Ni<sub>3</sub>S<sub>2</sub> catalyst and 5 mg carbon black was finally dispersed in ethanol (200 μL), and 25 μL 5 wt % Nafion solution. The mixed solution was followed by ultrasonication for 30 min to obtain a homogeneous catalyst suspension. Then 25 μL catalyst ink was dropped on the carbon cloth (loading area 0.5 cm × 0.5 cm) yielding a mass loading of 1.5 mg cm<sup>-2</sup>. The catalyst modified electrode was dried at 60 °C before electrochemical measurements. At least three identical electrodes for each electrocatalysts were made for the repeatability test.

### S1.4 Reference Electrode (RE) Calibration

We used Ag/AgCl as the reference electrode for all measurements. The calibration was performed in the high purity hydrogen saturated electrolyte with a Pt foil as the working electrode and counter electrode. CV were run at a scan rate of 1 mV s<sup>-1</sup> in 1 M KOH with/without 1 M methanol, and the average of the two potentials at which the current crossed zero was taken to be the thermodynamic potential for the hydrogen electrode reactions. The calibrated potentials measured against Ag/AgCl with RE calibration was convert to the reversible hydrogen electrode was calculated as follow:  $E(\text{RHE}) = E(\text{Ag/AgCl}) + 1.0205 \text{ V}$  (Fig. S5)[1, 2].

### S1.5 Catalyst Characterization

The Pt-Ni<sub>3</sub>S<sub>2</sub> catalyst were characterized by field emission transmission electron microscopy (FETEM) under the acceleration voltage of 200 kV and equipped with a EMSIS Xarosa CCD camera and Oxford INCA (Aztec) EDS detector at 20 kV with the potential of performing elemental analysis on the mode of dark field. To prepare the TEM specimens, one drop of the suspension was placed on a carbon film supported molybdenum grid and allowed to dry in air before the specimens were transferred into the microscope.

Crystallographic and purity information on Pt-Ni<sub>3</sub>S<sub>2</sub> catalyst were obtained using powder XRD. To analyze these materials, the as-synthesized samples (dispersed in isopropanol) after centrifugation were later air-dried upon deposition onto glass slides. Diffraction patterns of these materials were collected using a powder diffractometer (RIGAKU Smartlab) operating in the reflection mode equipped with a Ni filter and a Cu K $\alpha$  radiation ( $\lambda = 1.5406 \text{ \AA}$ ) source with the accelerating voltage of 40 kV and the applied current of 200 mA. The scanning is performed at 10 ° min<sup>-1</sup> from 10 ~ 80 ° with a step size of 0.02 °.

X-ray photoelectron spectroscopy (XPS) measurements were performed on a Thermo Scientific ESCALAB 250Xi spectrometer employing a monochromatic Al K $\alpha$  X-ray source ( $h\nu = 1486.8$  eV) and 500  $\mu\text{m}$  test spot area under 15 kV test tube voltage, 10 mA tube current, and  $2 \times 10^{-9}$  mbar room floor vacuum. The takeoff angle for the collection of photoelectrons was 90  $^\circ$  from the surface normal. Survey spectra were recorded on all samples followed by high resolution XPS spectra for Ni 2p, S 2p, Pt 2p and O 1s spectral regions. All the peaks were calibrated with C 1s spectrum at binding energy of 284.8 eV.

Ni K-edge X-ray absorption fine structure (XAFS) spectra of the Pt-Ni<sub>3</sub>S<sub>2</sub> catalyst were recorded by synchrotron radiation light source at the VESPERS beamline of the Canadian Light Source (CLS) with medium energy range of 6-30 keV. The catalysts were dispersed on Kapton (polyimide) tape for XAFS measurements using a four element vortex detector in the transmission mode at room temperature. The Si (111) crystal monochromator was utilized to acquire the scan for X-ray spectra, and the data was collected in the total electron yield (TEY) mode by measuring the sample drain current. The XAFS spectra include X-ray absorption near edge structure (XANES) and extended X-ray absorption fine structure (EXAFS). Energy calibration was performed with a standard nickel foil by shifting all spectra to a glitch in the incident intensity. Each spectrum was mathematically processed by a standard normalization method to exclude the influence of sample thickness, absorber concentration, detector, and amplifier settings. The k<sup>3</sup>-weighted Fourier transformation of EXAFS (FT-EXAFS) and the k<sup>2</sup>-weighted Wavelet transforms of the EXAFS (WT-EXAFS) spectra were made to obtain the information on local electronic structures and radial distribution environment of Ni atoms in Pt-Ni<sub>3</sub>S<sub>2</sub> catalyst.

## 1.6 Identification and Quantification of Formate Product

The identification and quantification of formate product are conducted by Ion Chromatography (IC) and determined by calibration curve. A small amount of electrolyte was taken by syringe after anode-cathode interchangeable electrocatalysis under ISTEP, and the electrolyte was properly diluted and consequently analyzed by Ion Chromatography (IC) to detect the formate generation. The Ion Chromatography (IC) was carried out on a CIC-D120 ion chromatograph (Shenghan Chromatography Technology Co., Ltd, Qingdao, China) equipped with an SH-AC-3 type anionic column. An aqueous solution containing sodium carbonate (2.4 mmol L<sup>-1</sup>) and sodium bicarbonate (6.0 mmol L<sup>-1</sup>) is employed as the eluent. The measurement is conducted at a constant temperature of 35  $^\circ\text{C}$  with a flow rate of 1.0 mL min<sup>-1</sup>. At least three accurate trace curves were collected for statistical analysis.

The identification and quantification of the formate products were determined by calibration curve by applying standard formate solutions with known concentrations of commercially purchased pure sodium formate (chromatographic pure) (Fig. S13a).

The Faradaic efficiency (FE) of formate generation was calculated using the following equation:

$$\text{FE}(\text{formate, \%}) = \frac{\text{mole of formed formate}}{\text{total charge passed} / (4 \times F)} \times 100\%$$

$$FE(\text{formate, \%}) = \frac{4 \times 96485 \left(\frac{\text{C}}{\text{mol}}\right) \times \omega_t \left(\frac{\text{mg}}{\text{L}}\right) \times V(\text{L}) \times 10^{-3} \left(\frac{\text{g}}{\text{mg}}\right)}{M_{\text{formate}} \left(\frac{\text{g}}{\text{mol}}\right) \times \int_0^t I(A) dt} \times 100\%$$

where

F is the Faraday constant (96485 C mol<sup>-1</sup>).

$\omega_t$ (mg L<sup>-1</sup>) is the concentration of formed formate in the electrolyte, namely, the IC data (ppm). The unit of ppm here is mass(formate)/volume(solution).

V(L) is the total volume of the electrolyte.

$M_{\text{formate}}$ (g mol<sup>-1</sup>) is the molecular weight of formate (HCOO<sup>-</sup>) equal to 45.02 g mol<sup>-1</sup>.

I(A) is the current recorded by the electrochemical workstation in the ISTEP mode.

### S1.7 Identification and Quantification of Gas Products

The generated H<sub>2</sub> from the electrolyzer were determined by gas chromatography (5977B MSD, Agilent Technologies) with a thermal conductivity detector (TCD). Argon (purity: 99.999%) was used as a carrier gas with a constant flow rate of 20 mL min<sup>-1</sup>. A stable flow rate of mixed gas (the gaseous products and the carrier gas) was achieved after a period of electrocatalytic reaction, which gave the accurate GC traces for measurements. The GC sampling was conducted at 1, 2, 3, 4, 5 and 6 hours of electrocatalytic reaction. The identification and quantification of the H<sub>2</sub> products were determined by calibration curve by applying commercial standard H<sub>2</sub> gas with known concentrations.

The generation rate (mol s<sup>-1</sup>) of H<sub>2</sub> was calculated using the following equation:

$$n_v(\text{H}_2, \text{mol/s}) = \frac{Vvp_0}{RT_0}$$

$$n_v(\text{H}_2, \text{mol/s}) = \frac{V\left(\frac{\text{m}^3}{\text{s}}\right) \times v(\text{vol ratio}) \times 1.01 \times 10^5 \left(\frac{\text{N}}{\text{m}^2}\right)}{8.314 \left(\frac{\text{N m}}{\text{mol K}}\right) \times 298.15(\text{K})}$$

where

v(vol ratio) is the volume concentration of H<sub>2</sub> in the exhaust gas from the electrolyzer, namely, the GC data (volume ppm). The unit of ppm here is volume(H<sub>2</sub>)/volume(total).

V(m<sup>3</sup> s<sup>-1</sup>) is the gas flow rate measured by a flow meter at room temperature and under ambient pressure.

The Faradaic efficiency (FE) of H<sub>2</sub> production was calculated using the following equation:

$$FE(\text{H}_2, \%) = \frac{\text{mole of formed H}_2}{\text{total charge passed} / (2 \times F)} \times 100\%$$

$$FE(\text{H}_2, \%) = \frac{2FVvp_0}{RT_0I} \times 100\%$$

$$FE(H_2, \%) = \frac{2 \times 96485 \left(\frac{C}{mol}\right) \times V\left(\frac{m^3}{s}\right) \times v(vol\ ratio) \times 1.01 \times 10^5 \left(\frac{N}{m^2}\right)}{8.314 \left(\frac{Nm}{mol\ K}\right) \times 298.15(K) \times I(A)} \times 100\%$$

where

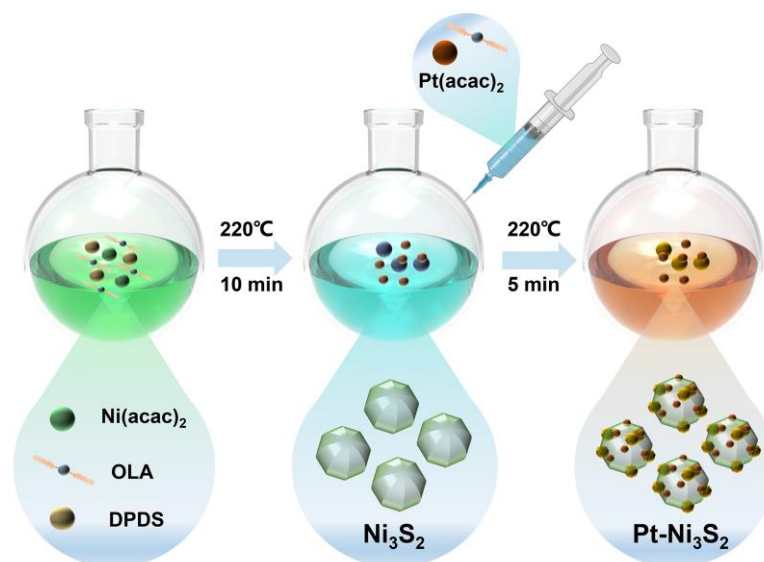
$F$  is the Faraday constant ( $96485\ C\ mol^{-1}$ ).

$v(vol\ ratio)$  is the volume concentration of  $H_2$  in the exhaust gas from the electrolyzer, namely, the GC data (volume ppm). The unit of ppm here is volume( $H_2$ )/volume(total).

$V(m^3\ s^{-1})$  is the gas flow rate measured by a flow meter at room temperature and under ambient pressure.

$I(A)$  is the current recorded by the electrochemical workstation in the ISTEP mode.

## S2 Supplementary Figures



**Scheme S1** Diagram of the synthesis of  $Ni_3S_2$  and  $Pt-Ni_3S_2$

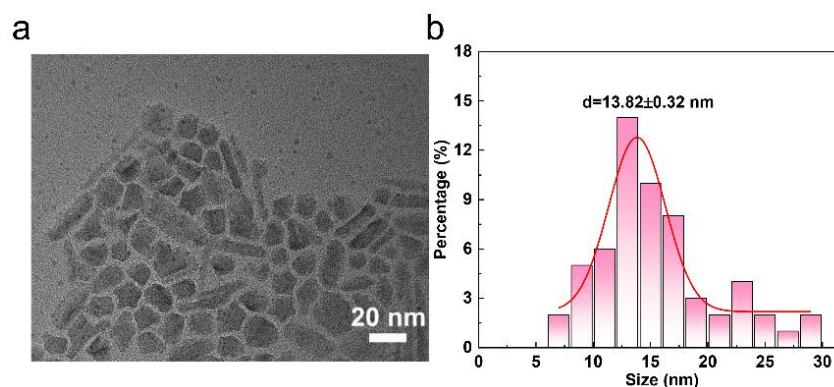


**Fig. S1** TEM image and size distribution plot clearly shows a monodispersed system with a particle size of  $13.82 \pm 0.32\ nm$  of  $Ni_3S_2$  nanocrystals

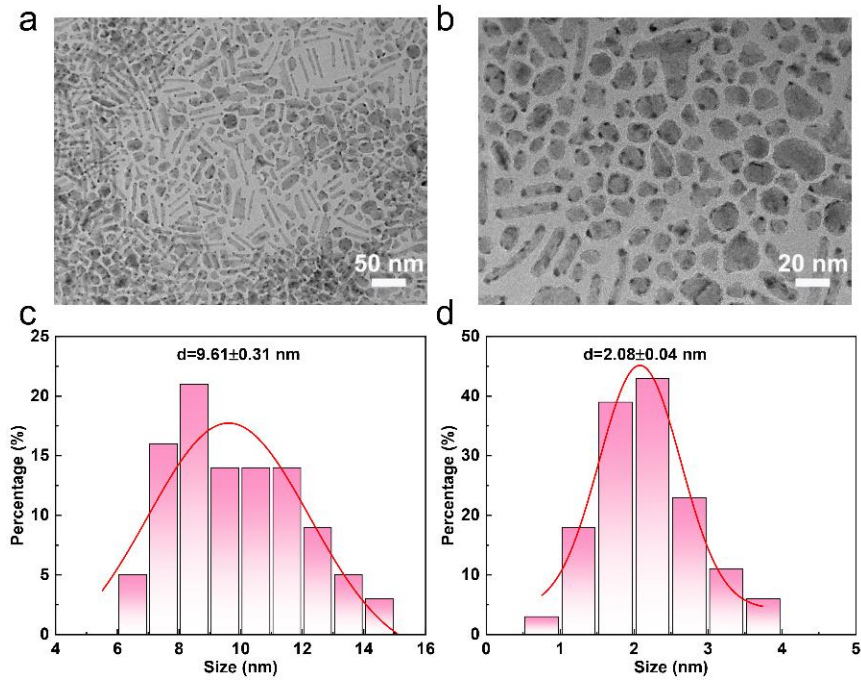


**Fig. S2** TEM image and size distribution plot clearly shows a dual-monodispersed system with a particle size of  $9.61 \pm 0.31$  nm of Pt-Ni<sub>3</sub>S<sub>2</sub> nanocrystals, in which, monodisperse Pt particles are only  $2.08 \pm 0.04$  nm in size

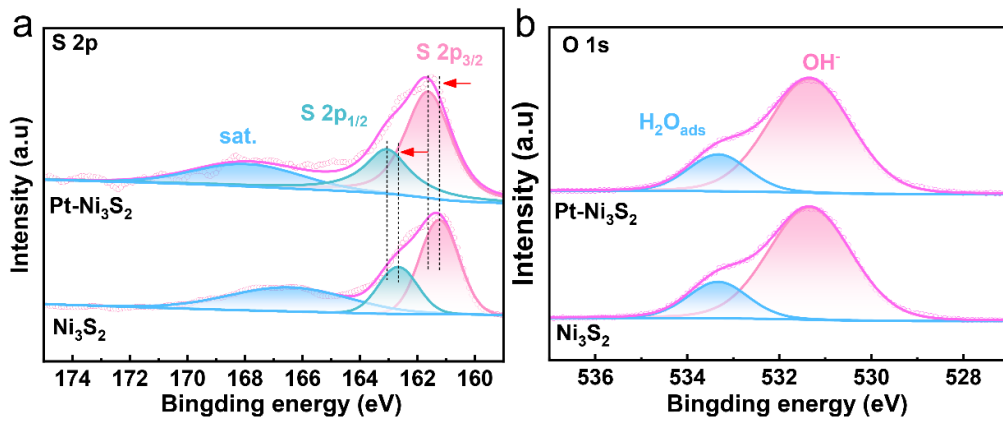


**Fig. S3** XPS of (a) S 2p and (b) O 1s of Pt-Ni<sub>3</sub>S<sub>2</sub> and Ni<sub>3</sub>S<sub>2</sub>

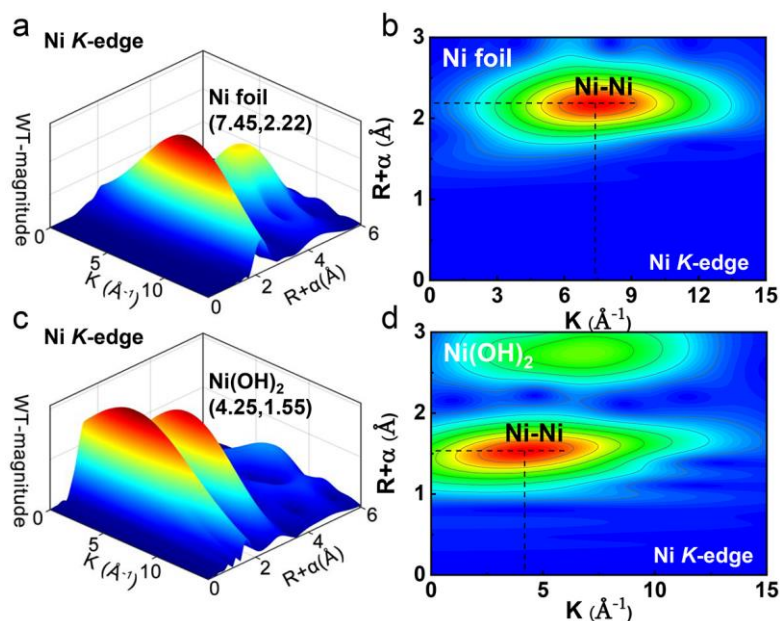


**Fig. S4** Wavelet transformed  $k^2$ -weighted EXAFS spectra (WT-EXAFS) and the corresponding 2D graphics of WT-EXAFS spectra about Ni for (a-b) Ni foil, (c-d) Ni(OH)<sub>2</sub>

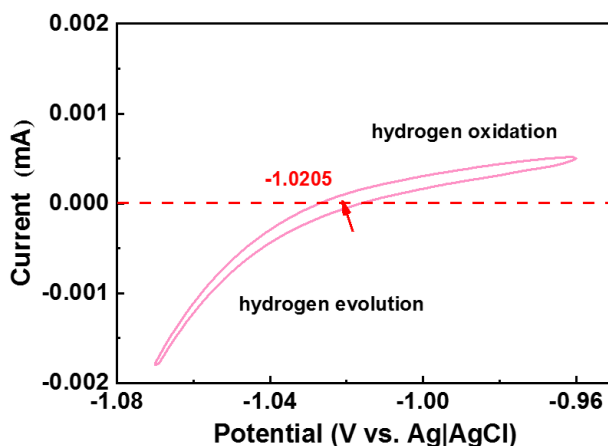


**Fig. S5** The calibration curve of Ag/AgCl in 1 mol L<sup>-1</sup> KOH with 1 mol L<sup>-1</sup> methanol

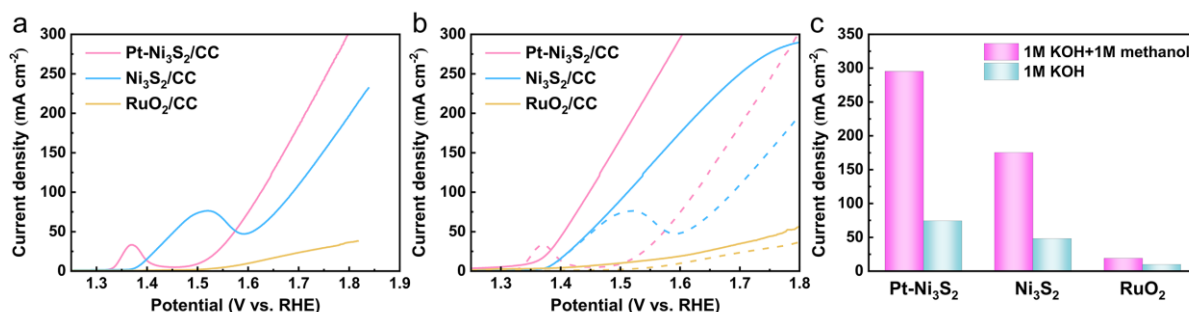


**Fig. S6** (a) LSV curves of Pt-Ni<sub>3</sub>S<sub>2</sub>/CC, Ni<sub>3</sub>S<sub>2</sub>/CC, RuO<sub>2</sub>/CC in 1.0 mol L<sup>-1</sup> KOH without  $iR$ -compensation; (b) LSV curves of Pt-Ni<sub>3</sub>S<sub>2</sub>/CC, Ni<sub>3</sub>S<sub>2</sub>/CC, RuO<sub>2</sub>/CC in 1.0 mol L<sup>-1</sup> KOH electrolyte with (solid lines)/without (dot-dash lines) the addition of 1.0 mol L<sup>-1</sup> methanol without  $iR$ -compensation. (c) The current density performance gap between MOR and OER at 1.6 V (vs. RHE)

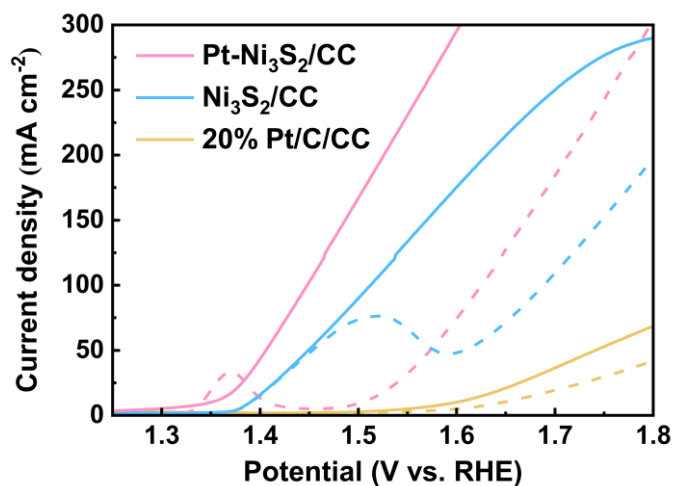


**Fig. S7** LSV curves of Pt-Ni<sub>3</sub>S<sub>2</sub>/CC, Ni<sub>3</sub>S<sub>2</sub>/CC, 20% Pt/C/CC in 1.0 mol L<sup>-1</sup> KOH electrolyte with (solid lines)/without (dot-dash lines) the addition of 1.0 mol L<sup>-1</sup> methanol without *iR*-compensation.

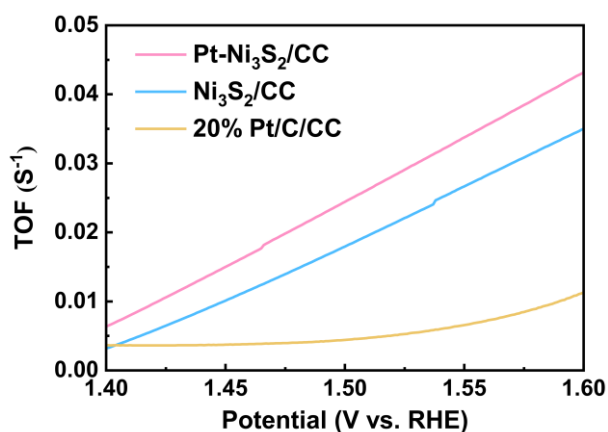


**Fig. S8** The turnover frequency of the Pt-Ni<sub>3</sub>S<sub>2</sub>/CC, Ni<sub>3</sub>S<sub>2</sub>/CC, 20% Pt/C/CC catalysts calculated from MOR polarization curves in 1.0 mol L<sup>-1</sup> KOH with 1.0 mol L<sup>-1</sup> methanol.

The values of TOF were calculated by assuming that all metal atoms are involved in the catalytic processes, which all represent the lowest limits of the models:

$$\text{TOF} = j * S / zFn$$

where  $j$  (mA cm<sup>-2</sup>) is the as-measured current density at various potentials,  $S$  (cm<sup>2</sup>) represents the surface area of the glassy carbon disk, the number  $z$  means a four-electron transfer during the formation of one mole of HCOOH for MOR (two-electron transfer during the formation of one mole of H<sub>2</sub> for HER),  $F$  is the Faraday's constant (96485.3 C mol<sup>-1</sup>), and  $n$  is the moles of Ni atoms on the electrode which can be calculated by the loading weight and the molecular weight of the coated catalysts.

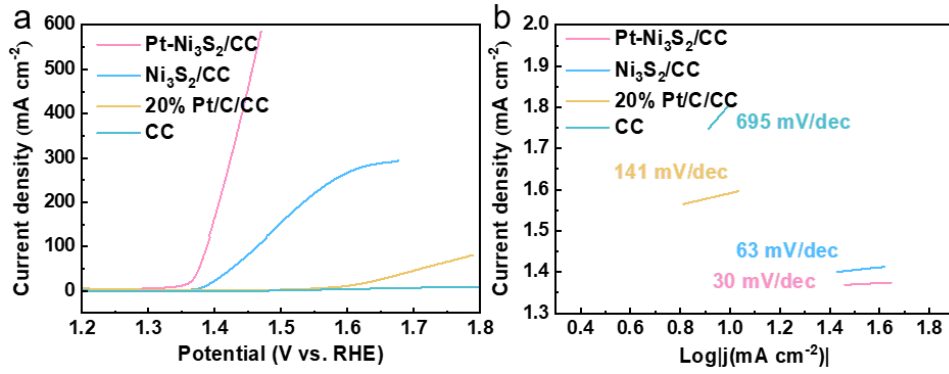


**Fig. S9** (a) LSV curves and (b) Tafel slope of Pt-Ni<sub>3</sub>S<sub>2</sub>/CC, Ni<sub>3</sub>S<sub>2</sub>/CC, 20% Pt/C/CC and pristine carbon cloth (CC) in 1.0 mol L<sup>-1</sup> KOH containing 1.0 mol L<sup>-1</sup> methanol with *iR*-compensation.

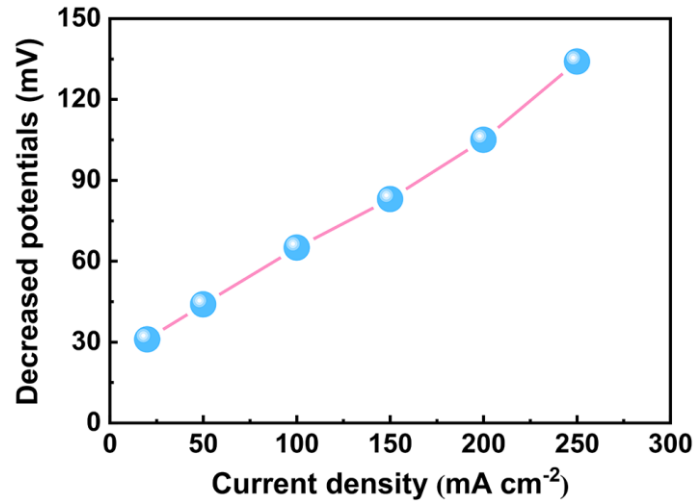


**Fig. S10** The decreased oxidative potentials of methanol upgrading reaction using Pt-Ni<sub>3</sub>S<sub>2</sub>/CC electrode at certain current densities compared with Ni<sub>3</sub>S<sub>2</sub>/CC electrode

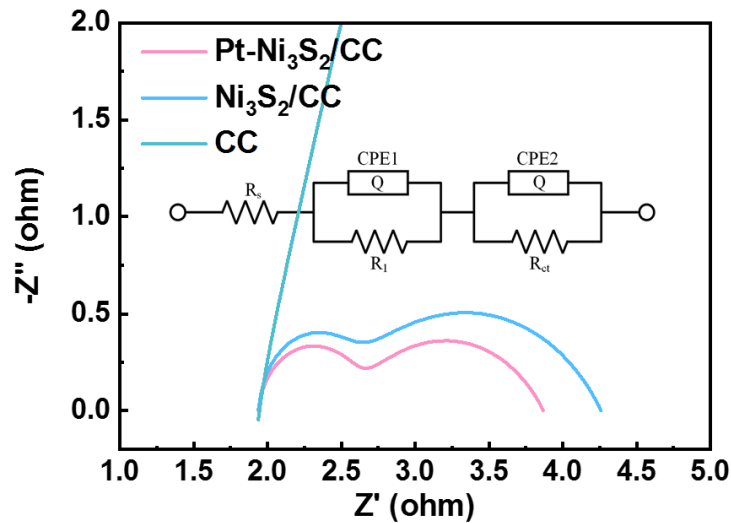


**Fig. S11** EIS of Pt-Ni<sub>3</sub>S<sub>2</sub>/CC, Ni<sub>3</sub>S<sub>2</sub>/CC and pristine carbon cloth (CC) in 1.0 mol L<sup>-1</sup> KOH containing 1.0 mol L<sup>-1</sup> methanol

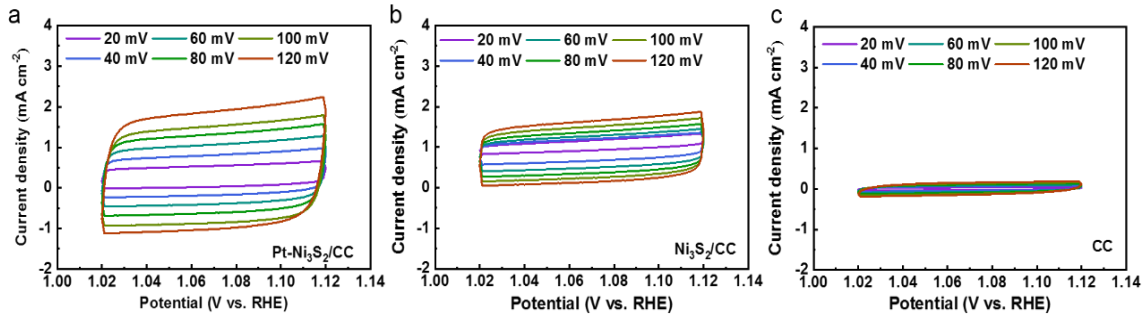


**Fig. S12** Cyclic voltammetry curves of (a) Pt-Ni<sub>3</sub>S<sub>2</sub>/CC, (b) Ni<sub>3</sub>S<sub>2</sub>/CC, (c) pristine CC at different scan rates from 20 to 120 mV s<sup>-1</sup> in 1.0 mol L<sup>-1</sup> KOH containing 1.0 mol L<sup>-1</sup> methanol

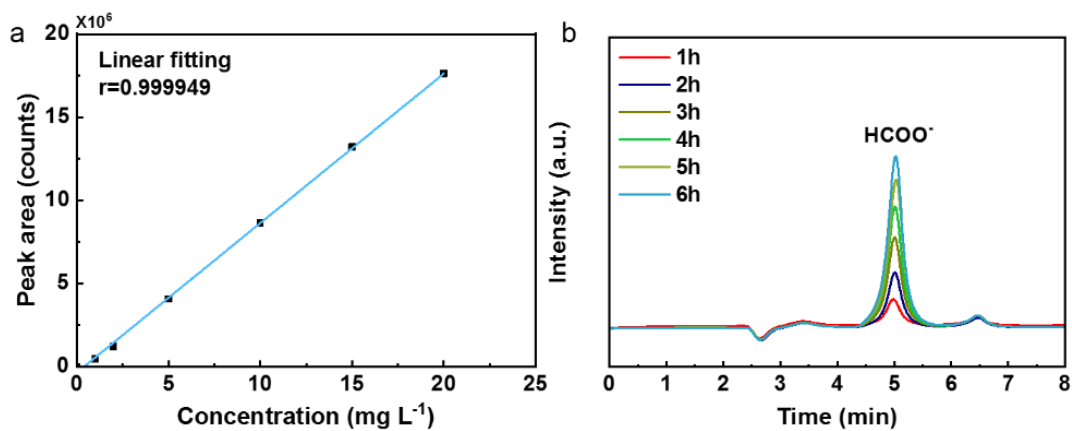


**Fig. S13** (a) The establishment of formate calibration curve by linear fitting based on the IC chromatogram traces. (b) IC traces for detecting the formate concentration in the electrolyte (1.0 mol L<sup>-1</sup> KOH + 1.0 mol L<sup>-1</sup> formate) after the 6 hours' MOR with Pt-Ni<sub>3</sub>S<sub>2</sub>/CC anode

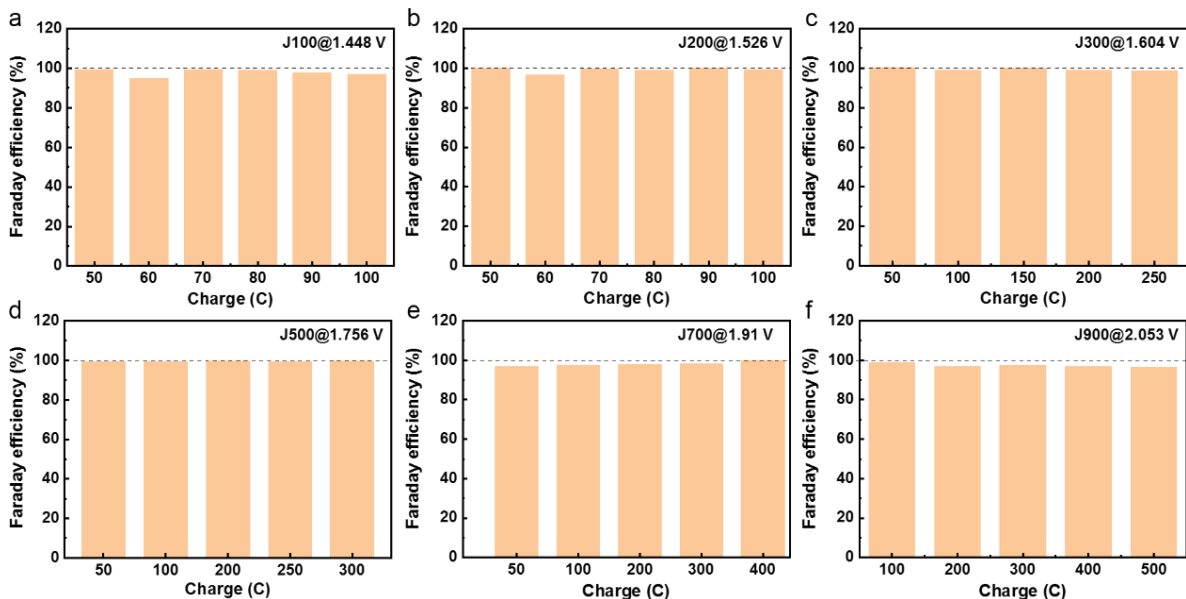


**Fig. S14** Faraday efficiency at different voltages (a) 1.448 V at 100 mA cm<sup>-2</sup>, (b) 1.526 V at 200 mA cm<sup>-2</sup>, (c) 1.604 V at 300 mA cm<sup>-2</sup>, (d) 1.756 V at 500 mA cm<sup>-2</sup>, (e) 1.91 V at 700 mA cm<sup>-2</sup>, (f) 2.053 V at 900 mA cm<sup>-2</sup>

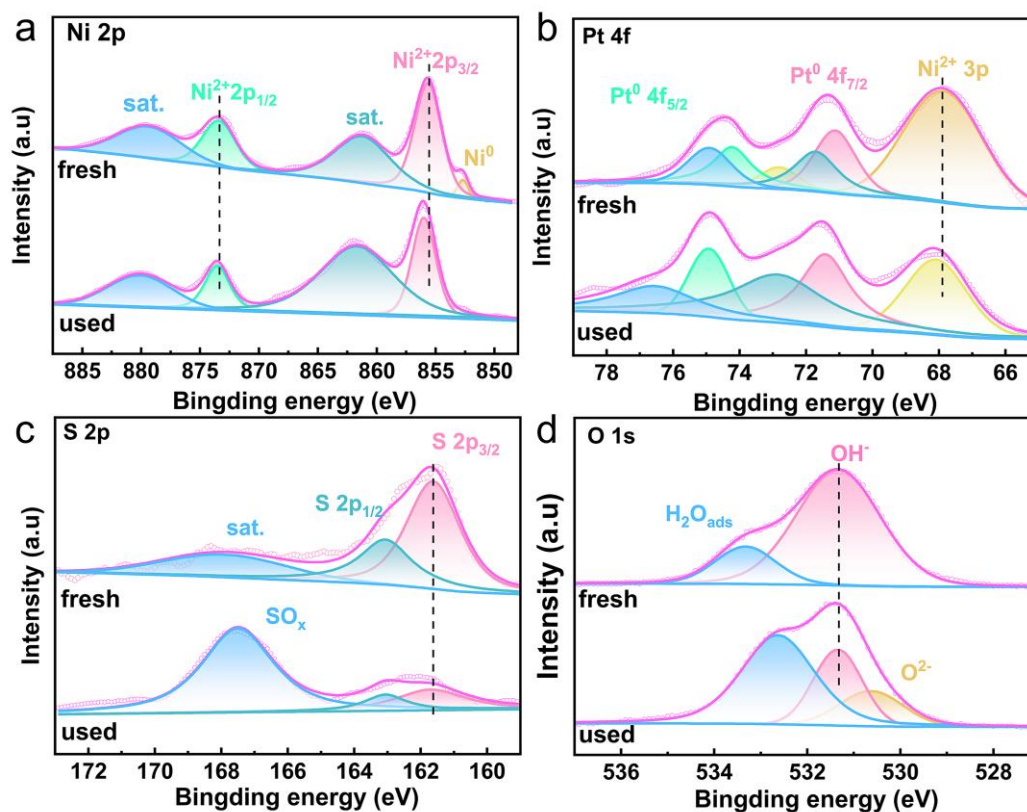


**Fig. S15** High-resolution XPS spectra. The comparison of fresh and used Pt-Ni<sub>3</sub>S<sub>2</sub> nano-heterostructures in (a) Ni 2p, (b) Pt 4f, (c) S 2p and (d) O 1s regions after MOR stability tests by chronoamperometry (*I-t*) at 2.12 V (vs. RHE) with an initial current density of ~1000 mA cm<sup>-2</sup> for 72 h

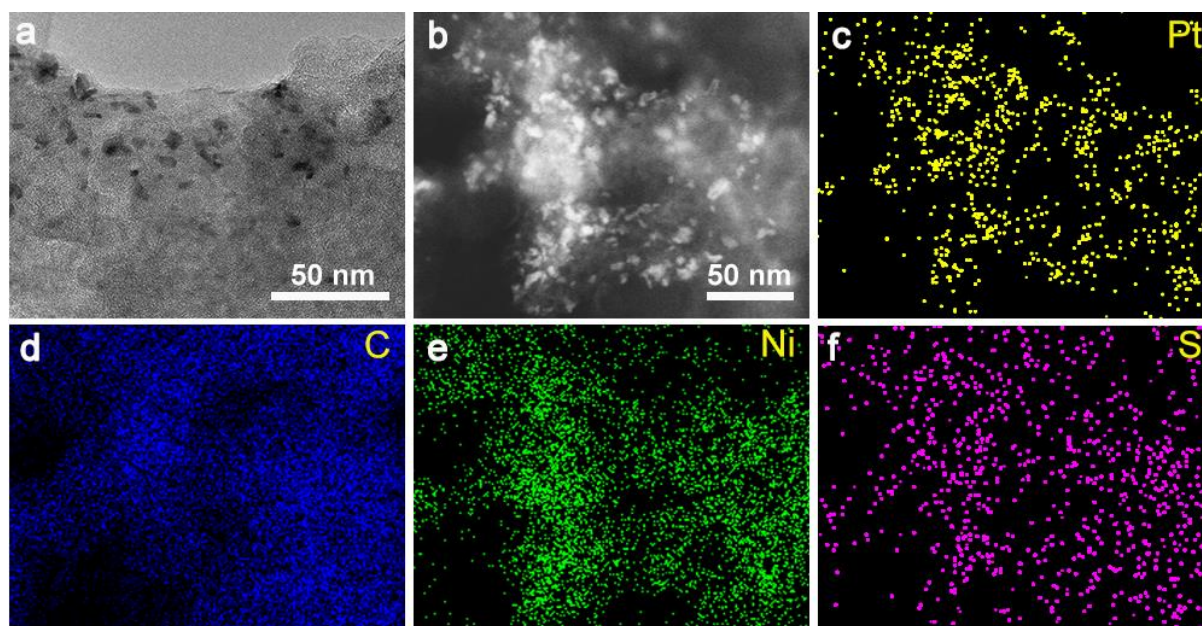


**Fig. S16** (a) HRTEM images; (b) HAADF-STEM image and the corresponding EDS elemental (c-f) mapping images of Pt-Ni<sub>3</sub>S<sub>2</sub> nano-heterostructures after MOR stability tests by chronoamperometry (*I-t*) at 2.12 V (vs. RHE) with an initial current density of ~1000 mA cm<sup>-2</sup> for 72 h

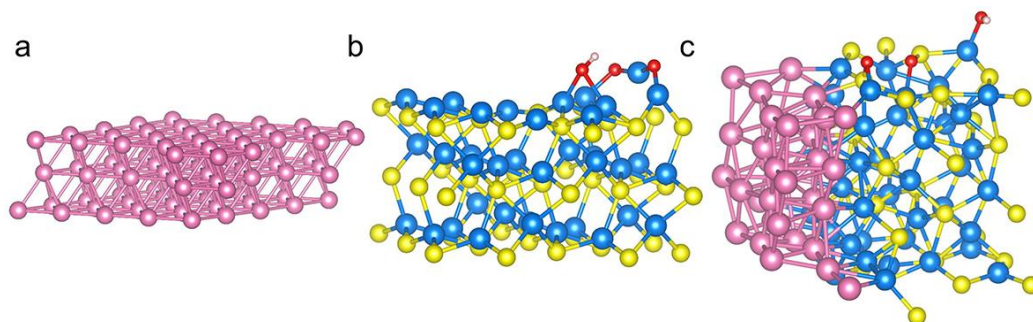


**Fig. S17** The computational models of (a) Pt, (b) Ni<sub>3</sub>S<sub>2</sub> and (c) Pt-Ni<sub>3</sub>S<sub>2</sub> about MOR

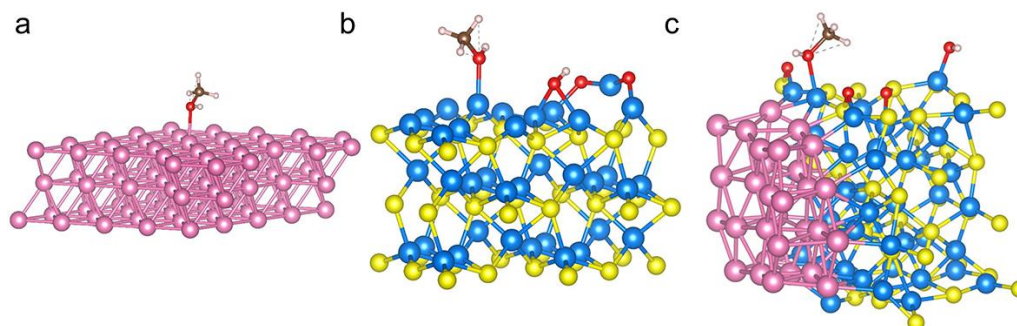


**Fig. S18** CH<sub>3</sub>OH binding models of (a) Pt, (b) Ni<sub>3</sub>S<sub>2</sub> and (c) Pt-Ni<sub>3</sub>S<sub>2</sub>

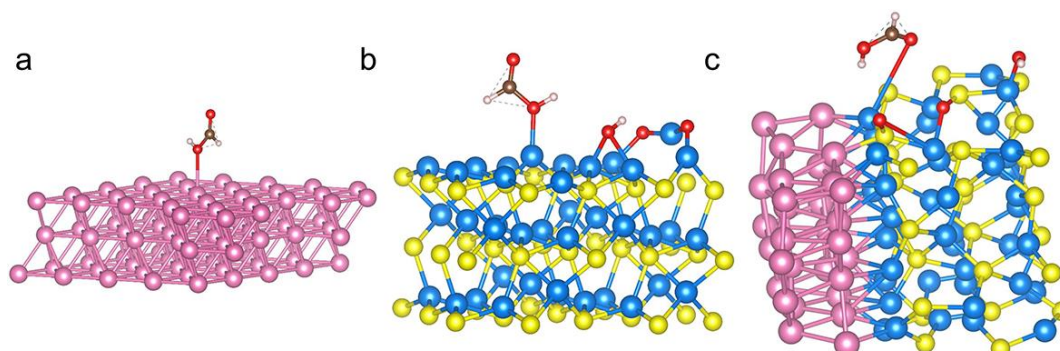


**Fig. S19** HCOOH binding models of (a) Pt, (b) Ni<sub>3</sub>S<sub>2</sub> and (c) Pt-Ni<sub>3</sub>S<sub>2</sub>

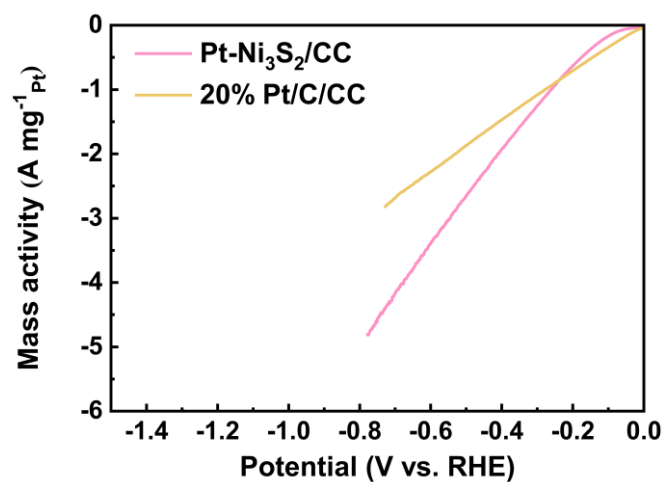


**Fig. S20** The electrocatalytic performance about mass activity with Pt-Ni<sub>3</sub>S<sub>2</sub>/CC, and 20% Pt/C/CC

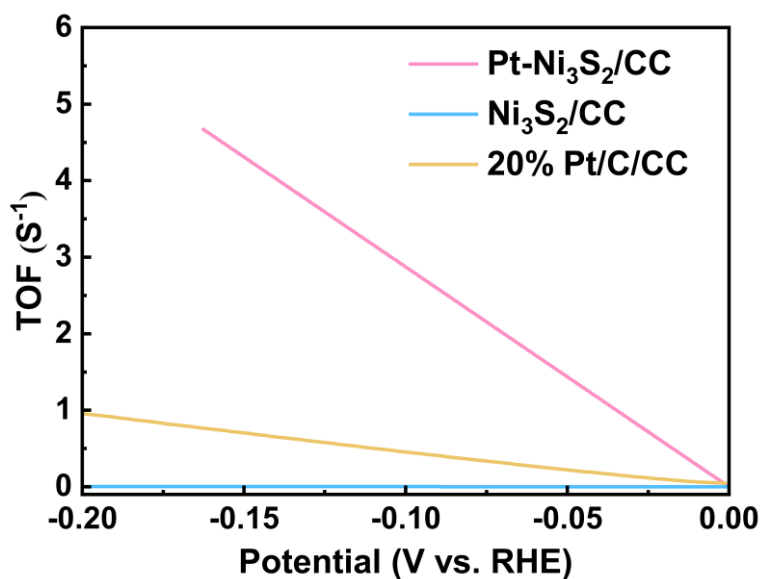


**Fig. S21** The turnover frequency of the Pt-Ni<sub>3</sub>S<sub>2</sub>/CC, Ni<sub>3</sub>S<sub>2</sub>/CC, 20% Pt/C/CC catalysts calculated from HER polarization curves in 1.0 mol L<sup>-1</sup> KOH

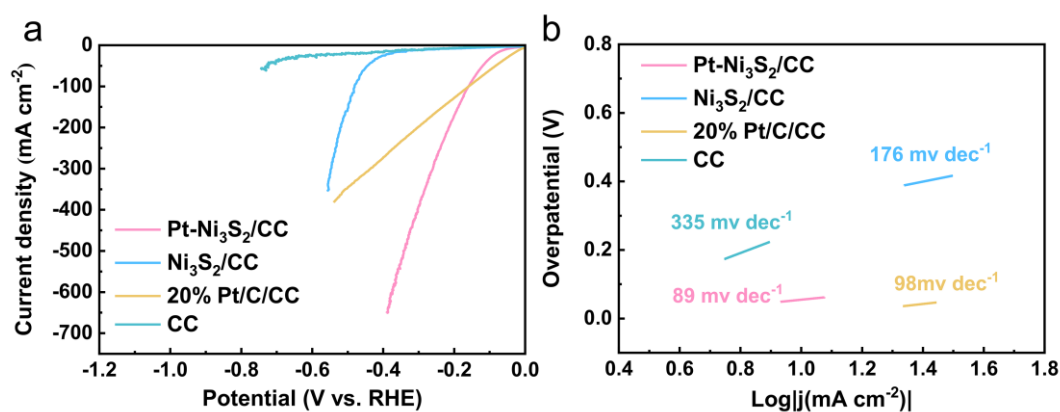


**Fig. S22** (a) LSV curves and (b) Tafel slope plots of Pt-Ni<sub>3</sub>S<sub>2</sub>/CC, Ni<sub>3</sub>S<sub>2</sub>/CC, 20% Pt/C/CC and pristine carbon cloth (CC) in 1.0 mol L<sup>-1</sup> KOH with  $iR$ -compensation

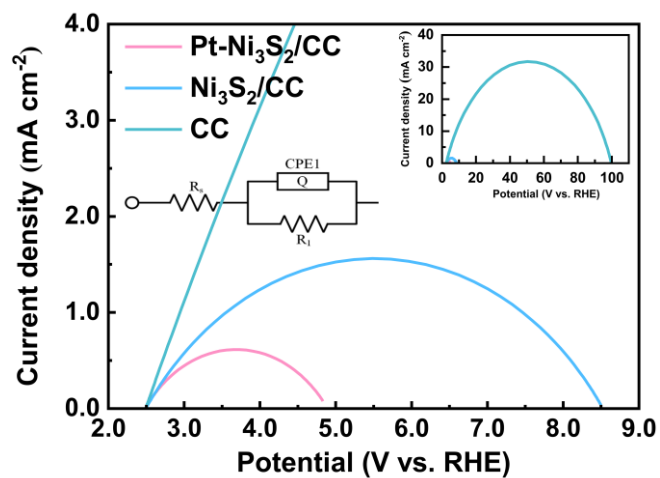


**Fig. S23** EIS curves of Pt-Ni<sub>3</sub>S<sub>2</sub>/CC, Ni<sub>3</sub>S<sub>2</sub>/CC and pristine carbon cloth (CC) in 1.0 mol L<sup>-1</sup> KOH

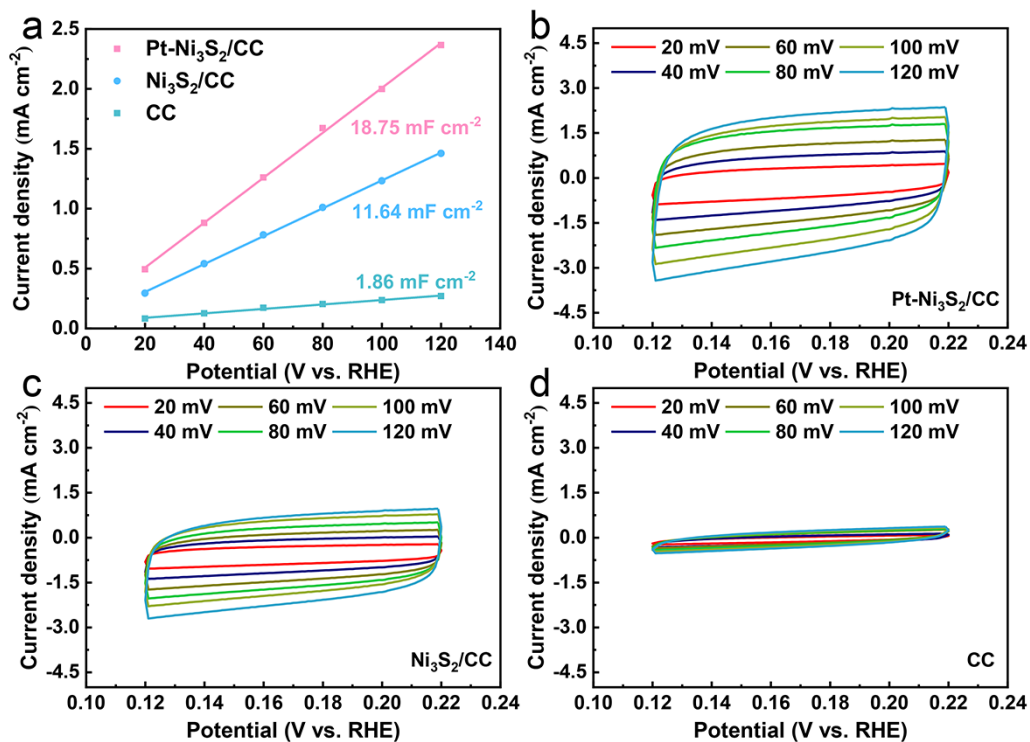


**Fig. S24** (a) Calculated electrochemical double-layer capacitances ( $C_{dl}$ ) of Pt-Ni<sub>3</sub>S<sub>2</sub>/CC, Ni<sub>3</sub>S<sub>2</sub>/CC, CC, Cyclic voltammetry curves of (b) Pt-Ni<sub>3</sub>S<sub>2</sub>/CC, (c) Ni<sub>3</sub>S<sub>2</sub>CC, (d) pristine CC at different scan rates from 20 to 120 mV s<sup>-1</sup> in 1.0 mol L<sup>-1</sup> KOH

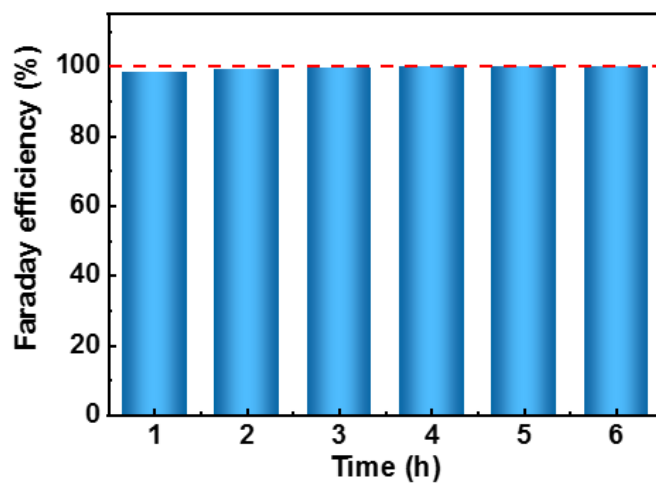


**Fig. S25** The corresponding faradaic efficiencies for H<sub>2</sub> generation in 1.0 mol L<sup>-1</sup> KOH

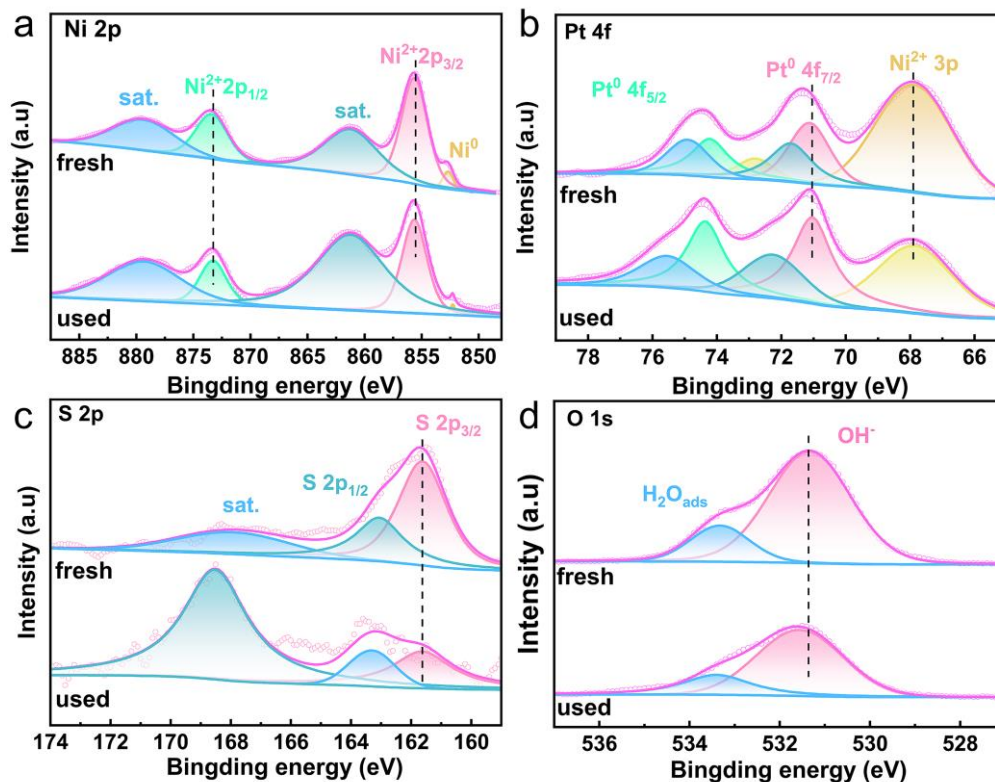


**Fig. S26** High-resolution XPS spectra. The comparison of fresh and used Pt-Ni<sub>3</sub>S<sub>2</sub> nano-heterostructures in (a) Ni 2p, (b) Pt 4f, (c) S 2p and (d) O 1s regions after HER stability tests by chronoamperometry (*I-t*) with current density of 100 mA cm<sup>-2</sup> for 24 h

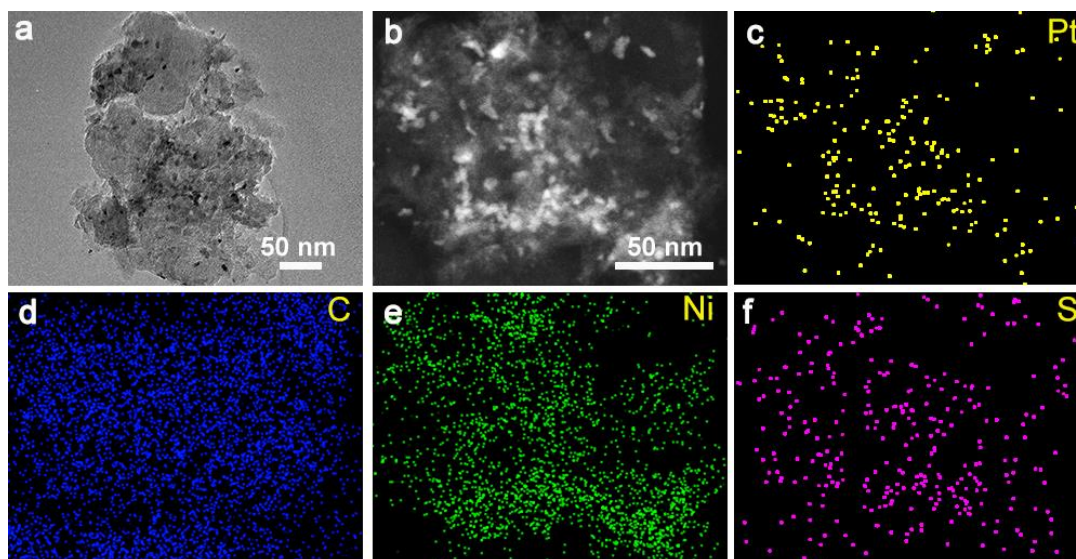


**Fig. S27** (a) HRTEM images; (b) HAADF-STEM image and the corresponding EDS elemental (c-f) mapping images of Pt-Ni<sub>3</sub>S<sub>2</sub> nano-heterostructures after HER stability tests by chronoamperometry (*I-t*) with current density of 100 mA cm<sup>-2</sup> for 24 h

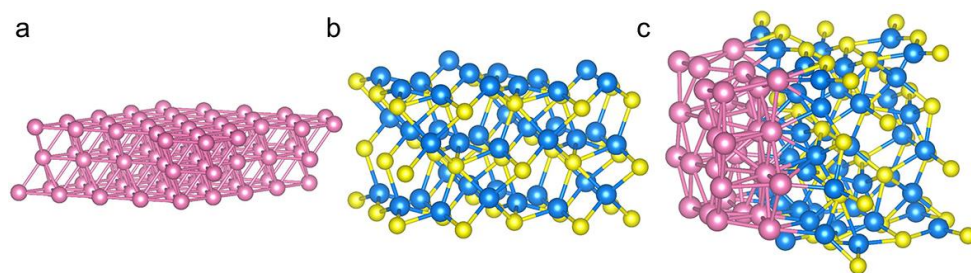


**Fig. S28** The computational models of (a) Pt, (b) Ni<sub>3</sub>S<sub>2</sub> and (c) Pt-Ni<sub>3</sub>S<sub>2</sub> about HER

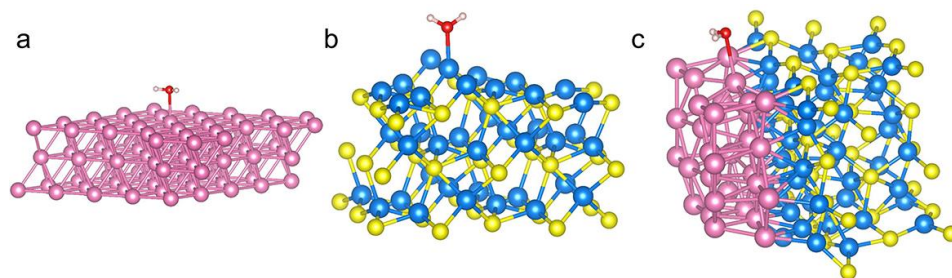


**Fig. S29** H<sub>2</sub>O binding models of (a) Pt, (b) Ni<sub>3</sub>S<sub>2</sub> and (c) Pt-Ni<sub>3</sub>S<sub>2</sub>

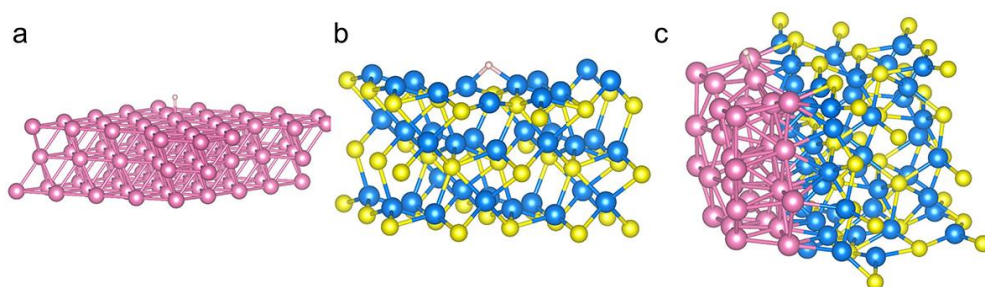


**Fig. S30** H binding models of (a) Pt, (b) Ni<sub>3</sub>S<sub>2</sub> and (c) Pt-Ni<sub>3</sub>S<sub>2</sub>

### 3 Supplementary Tables

**Table S1** Element content analysis of Pt-Ni<sub>3</sub>S<sub>2</sub> via ICP-MS.

Element	Mass Fraction (%)	Atom ratio
Ni	69.67	1.18
Pt	9.38	0.05
S	20.96	0.66

**Table S2** Fitting impedance parameters of various catalysts for MOR

Catalysts	R <sub>s</sub> (Ω)	R <sub>ct1</sub> (Ω)	R <sub>ct2</sub> (Ω)
Pt-Ni <sub>3</sub> S <sub>2</sub> /CC	2.391	0.634	1.297
Ni <sub>3</sub> S <sub>2</sub> /CC	1.936	0.529	1.795

**Table S3** Fitting impedance parameters of various catalysts for HER

Catalysts	$R_s$ ( $\Omega$ )	$R_{ct}$ ( $\Omega$ )
Pt-Ni <sub>3</sub> S <sub>2</sub> /CC	2.392	2.408
Ni <sub>3</sub> S <sub>2</sub> /CC	2.494	6.031

**Table S4** MOR activities of Pt-Ni<sub>3</sub>S<sub>2</sub> compared with those of Pt-based, Ni-based and S-based materials reported previously.

Electrocatalyst	Electrolyte	Potential@10 mA cm <sup>-2</sup> (V vs. RHE)	Potential@100 mA cm <sup>-2</sup> (V vs. RHE)	Peak current density, mass activity, or stability test	Refs.
<b>Pt-Ni<sub>3</sub>S<sub>2</sub></b>	<b>1.0 M KOH + 1.0 M MeOH</b>	<b>1.35</b>	<b>1.448</b>	<b>&gt; 700 mA cm<sup>-2</sup> (equivalent to &gt; 5.18 A mg<sup>-1</sup>) after 72 hours' reaction by <i>I-t</i></b>	<b>This work</b>
Ni-based	Ni <sub>3</sub> C	1.0 M KOH + 1.0 M MeOH	~1.39	~1.6	[S3]
	NiP <sub>x</sub> -R	1.0 M KOH + 0.5 M MeOH	~1.36	1.49	[S4]
	NiS <sub>x</sub> -R	1.0 M KOH + 0.5 M MeOH	~1.362	~1.51	[S4]
	NiSe <sub>x</sub> -R	1.0 M KOH + 0.5 M MeOH	~1.38	~1.53	[S4]
	Ni <sub>0.75</sub> Fe <sub>0.25</sub> Se <sub>2</sub>	1.0 M KOH + 0.5 M MeOH	1.40	~1.58	[S5]
	NiB-400	1.0 M KOH + 1.0 M MeOH	~1.38	~1.51	[S6]
	CuONS/CF	1.0 M KOH + 1.0 M MeOH	~1.37	1.50	[S7]
	Ni <sub>3</sub> B/Ni	1.0 M KOH + 1.0 M MeOH	~1.38	1.526	[S8]
	Ni polyhedral NCs	1.0 M KOH + 1.0 M MeOH	~1.5	~1.6	[S9]
Pt-based	Pt <sub>1</sub> /RuO <sub>2</sub>	0.1 M KOH + 1.0 M MeOH		6.766 A mg <sup>-1</sup> from CV/LSV at 50 mV s <sup>-1</sup> , absence of <i>I-t</i> or CP tests	[S10]
	Pt/Ni(OH) <sub>2</sub> /rGO	1.0 M KOH + 1.0 M MeOH		< 0.2 A mg <sup>-1</sup> after 55.56 hours' reaction by <i>I-t</i>	[S11]
	NiPtSAA/GDY	1.0 M KOH + 1.0 M MeOH		< 25 mA cm <sup>-2</sup> after 20 hours' reaction by <i>I-t</i>	[12]
	Pt <sub>3</sub> Bi <sub>3</sub> Zn	0.1 M HClO <sub>4</sub> + 0.5 M MeOH		3.29 A mg <sup>-1</sup> from CV/LSV at 20 mV s <sup>-1</sup> , absence of <i>I-t</i> or CP tests	[S13]
	Pt NPs trapped by CNTs	0.5 M H <sub>2</sub> SO <sub>4</sub> + 1.0 M MeOH		0.149 A mg <sup>-1</sup> from CV/LSV at 50 mV s <sup>-1</sup> , < 0.002 mA	[S14]

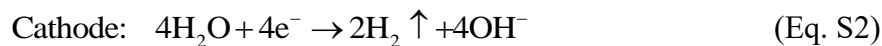
		cm <sup>-2</sup> after 0.5 hour's reaction by <i>I-t</i>		
	Pt/bTNT5	0.1 M HClO <sub>4</sub> + 0.5 M MeOH	< 70 mA cm <sup>-2</sup> after 1 hour's reaction by <i>I-t</i>	[S15]
S-based	Ni(OH) <sub>2</sub> Ni <sub>3</sub> S <sub>4</sub>	1.0 M KOH + 0.5 M MeOH	1.61	[S16]
	NiS <sub>x</sub> -R	1.0 M KOH + 0.5 M MeOH	~1.362      ~1.51	[S4]

**Table S5** HER activities of Pt-Ni<sub>3</sub>S<sub>2</sub> should be compared with those of Pt-based, Ni-based and S-based materials reported previously

	Electrocatalyst	Electrocatalyst	Potential@10 mA cm-2 (V vs. RHE)	Refs.
	<b>Pt-Ni<sub>3</sub>S<sub>2</sub></b>	<b>1.0 M KOH</b>	<b>60</b>	<b>This work</b>
Ni-based	Au/Ni <sub>3</sub> S <sub>2</sub>	1.0 M KOH	97	[S17]
	Ni <sub>3</sub> S <sub>2</sub> /MnS-O	1.0 M KOH	116	[S18]
	CoNi <sub>2</sub> S <sub>4</sub> /Ni <sub>3</sub> S <sub>2</sub>	1.0 M KOH	171	[S19]
	δ-FeOOH/Ni <sub>3</sub> S <sub>2</sub>	1.0 M KOH	106	[S20]
	NC@NiNPs	1.0 M KOH	74	[S21]
Pt-based	Pt <sub>4</sub> /s-MoO <sub>3</sub>	1.0 M KOH	123	[S22]
	Pt <sub>85</sub> Mo <sub>15</sub> -Se NWs	0.1 M NaOH	>> 100 mV	[S23]
S-based	NiWO <sub>4</sub> -Ni <sub>3</sub> S <sub>2</sub>	1.0 M KOH	136	[S24]
	Fe-Mo-S/Ni <sub>3</sub> S <sub>2</sub>	1.0 M KOH	141	[S25]

## S4 Equations

In 1.0 mol L<sup>-1</sup> KOH with 1.0 mol L<sup>-1</sup> methanol, the equations describe the anode, cathode and overall electrochemical reactions are proposed as follows, respectively.





In the alkaline electrolyte, the formation of one mole formate will consume five-fold amount of hydroxyl ions in the anode compartment (Equation S1), which is a four-electron transfer process. Accordingly, four moles of electrons will react with 4 moles of water molecules at the cathode to form 2 moles of H<sub>2</sub> gas and 4 moles of hydroxyl ions (Equation S2).

Since the generation of formate in alkaline environment will consume the hydroxyl ions, the pH of the electrolyte will be decreased along with the production of formate. The results also indicate that the high alkaline concentration is beneficial for the high reactivity of methanol upgrading reaction.

## Supplementary References

- [S1] S. Niu, S. Li, Y. Du, X. Han, P. Xu. How to reliably report the overpotential of an electrocatalyst. *ACS Energy Lett.* **5**, 1083-1087 (2020).  
<https://doi.org/10.1021/acseenergylett.0c00321>
- [S2] L. H. Sun, Q. Y. Li, S. N. Zhang, D. Xu, Z. H. Xue et al. Heterojunction-based electron donors to stabilize and activate ultrafine Pt nanoparticles for efficient hydrogen atom dissociation and gas evolution. *Angew. Chem. Int. Ed.* **60**, 25766-25770 (2021).  
<https://doi.org/10.1002/anie.202111920>
- [S3] J. S. Li, R. L. Wei, X. Wang, Y. Zuo, X. Han et al. Selective methanol-to-formate electrocatalytic conversion on branched nickel carbide. *Angew. Chem. Int. Ed.* **59**, 20826-20830 (2020). <https://doi.org/10.1002/anie.202004301>
- [S4] S. L. Li, R. G. Ma, J. C. Hu, Z. C. Li, L. J. Liu et al. Coordination environment tuning of nickel sites by oxyanions to optimize methanol electro-oxidation activity. *Nat. Commun.* **13**, 2916 (2022). <https://doi.org/10.1038/s41467-022-30670-4>
- [S5] J. Li, C. Xing, Y. Zhang, T. Zhang, M. C. Spadaro et al. Nickel iron diselenide for highly efficient and selective electrocatalytic conversion of methanol to formate. *Small* **17**, e2006623 (2021). <https://doi.org/10.1002/smll.202006623>
- [S6] Y. B. Qi, Y. Zhang, L. Yang, Y. H. Zhao, Y. H. Zhu et al. Insights into the activity of nickel boride/nickel heterostructures for efficient methanol electrooxidation. *Nat. Commun.* **13**, 4602 (2022). <https://doi.org/10.1038/s41467-022-32443-5>
- [S7] X. F. Wei, Y. Li, L. S. Chen, J. L. Shi. Formic acid electro-synthesis by concurrent cathodic CO<sub>2</sub> reduction and anodic ch<sub>3</sub>oh oxidation. *Angew. Chem. Int. Ed.* **60**, 3148-3155 (2021). <https://doi.org/10.1002/anie.202012066>
- [S8] Z. Liu, P. Chang, M. Xi, J. Ding, X. Wang et al. Synthesis of Ni(3) B/Ni via vacuum-induced for ultrahigh stable and efficient methanol oxidation. *Small* **23**, 2303855 (2023).  
<https://doi.org/10.1002/smll.202303855>
- [S9] J. Li, Y. Zuo, J. Liu, X. Wang, X. Yu et al. Superior methanol electrooxidation performance of (110)-faceted nickel polyhedral nanocrystals. *J. Mater. Chem. A* **7**,

- 22036-22043 (2019). <https://doi.org/10.1039/c9ta07066d>
- [S10] Z. Q. Zhang, J. P. Liu, J. Wang, Q. Wang, Y. H. Wang et al. Single-atom catalyst for high-performance methanol oxidation. *Nat. Commun.* **12**, 5235 (2021). <https://doi.org/10.1038/s41467-021-25562-y>
- [S11] W. Huang, H. Wang, J. Zhou, J. Wang, P. N. Duchesne et al. Highly active and durable methanol oxidation electrocatalyst based on the synergy of platinum-nickel hydroxide-graphene. *Nat. Commun.* **6**, 10035 (2015). <https://doi.org/10.1038/ncomms10035>
- [S12] L. Hui, Y. R. Xue, C. Y. Xing, Y. X. Liu, Y. C. Du et al. Atomic alloys of nickel-platinum on carbon network for methanol oxidation. *Nano Energy* **95**, 106984 (2022). <https://doi.org/10.1016/j.nanoen.2022.106984>
- [S13] H. Tian, D. Wu, J. Li, J. Luo, C. Jia et al. Rational design ternary platinum based electrocatalysts for effective methanol oxidation reaction. *J. Energy Chem.* **70**, 230-235 (2022). <https://doi.org/10.1016/j.jechem.2022.02.021>
- [S14] P. R. M, S. Berchmans. Electrochemically activated platinum nanoparticles trapped by carbon nanotubes for methanol oxidation reaction. *J. Electroanal. Chem.* **940**, 117492 (2023). <https://doi.org/10.1016/j.jelechem.2023.117492>
- [S15] A. Touni, X. Liu, X. Kang, C. Papoulia, E. Pavlidou et al. Methanol oxidation at platinum coated black titania nanotubes and titanium felt electrodes. *Molecules.* **27**, 6382 (2022). <https://doi.org/10.3390/molecules27196382>
- [S16] C. Hou, W. Yang, X. Yang, B. Li, H. Gao et al. In situ sulfidation for controllable hetero-interface engineering of  $\alpha$ -Ni(OH)<sub>2</sub>-Ni<sub>3</sub>S<sub>4</sub> hybrid structures realizing robust electrocatalytic methanol oxidation. *Chem. Commun.* **56**, 5283-5286 (2020). <https://doi.org/10.1039/d0cc01298j>
- [S17] H. Liu, J. N. Cheng, W. J. He, Y. Li, J. Mao et al. Interfacial electronic modulation of Ni<sub>3</sub>S<sub>2</sub> nanosheet arrays decorated with au nanoparticles boosts overall water splitting. *Appl. Catal. B Environ.* **304**, 120935 (2022). <https://doi.org/10.1016/j.apcatb.2021.120935>
- [S18] Y. Zhang, J. Fu, H. Zhao, R. Jiang, F. Tian et al. Tremella-like Ni<sub>3</sub>S<sub>2</sub>/mns with ultrathin nanosheets and abundant oxygen vacancies directly used for high speed overall water splitting. *Appl. Catal. B Environ.* **257**, 117899 (2019). <https://doi.org/10.1016/j.apcatb.2019.117899>
- [S19] W. Dai, K. Ren, Y.-a. Zhu, Y. Pan, J. Yu et al. Flower-like CoNi<sub>2</sub>S<sub>4</sub>/Ni<sub>3</sub>S<sub>2</sub> nanosheet clusters on nickel foam as bifunctional electrocatalyst for overall water splitting. *J. Alloys Compd.* **844**, 156252 (2020). <https://doi.org/10.1016/j.jallcom.2020.156252>
- [S20] X. Ji, C. Cheng, Z. Zang, L. Li, X. Li et al. Ultrathin and porous  $\delta$ -FeOOH modified Ni<sub>3</sub>S<sub>2</sub> 3D heterostructure nanosheets with excellent alkaline overall water splitting performance. *J. Mater. Chem. A* **8**, 21199-21207 (2020). <https://doi.org/10.1039/d0ta07676g>
- [S21] T. Yang, L. Fan, L. Wenqian, M. Shaoli, L. Xiaohong et al. Multifunctional carbon-

armored ni electrocatalyst for hydrogen evolution under high current density in alkaline electrolyte solution. *Appl. Catal. B Environ.* **321**, 122081 (2022).

<https://doi.org/10.1016/j.apcatb.2022.122081>

- [S22] T. Peng, H. Po-Yuan, E. N. S. Jack, W. Chenbo, G. Diego et al. Structure–property relationship of defect-trapped Pt single-site electrocatalysts for the hydrogen evolution reaction. *ACS Catal.* **13**, 9558-9566 (2023). <https://doi.org/10.1021/acscatal.3c01513>
- [S23] L. Yu, T. Zhou, S. Cao, X. Tai, L. Liu et al. Suppressing the surface passivation of Pt-Mo nanowires via constructing Mo-Se coordination for boosting her performance. *Nano Res.* **1-7**, (2020). <https://doi.org/10.1007/s12274-020-3269-8>
- [S24] S. Huang, Y. Meng, Y. Cao, F. Yao, Z. He et al. Amorphous NiWO<sub>4</sub> nanoparticles boosting the alkaline hydrogen evolution performance of Ni<sub>3</sub>S<sub>2</sub> electrocatalysts. *Appl. Catal. B Environ.* **274**, 119120 (2020). <https://doi.org/10.1016/j.apcatb.2020.119120>
- [S25] Y. Zhang, H. Guo, X. Li, J. Du, W. Ren et al. A 3D multi-interface structure of coral-like Fe-Mo-S/Ni<sub>3</sub>S<sub>2</sub>@NF using for high-efficiency and stable overall water splitting. *Chem. Eng. J.* **404**, 126483 (2020). <https://doi.org/10.1016/j.cej.2020.126483>